# Reduced graphene oxide supported tin oxide-boron oxide flexible paper anodes for Li-ion batteries

**Hilal KÖSE**[1,2,*] , **Şeyma DOMBAYCIOĞLU**[1,2] , **Hatem AKBULUT**[2,3] , **Ali Osman AYDIN**[1,2]

[1]Department of Chemistry, Faculty of Arts and Sciences, Sakarya University, Sakarya, Turkey
[2]Sakarya University Research, Development and Application Center (SARGEM), Sakarya, Turkey
[3]Department of Metallurgical and Material Engineering, Faculty of Engineering,
Sakarya University, Sakarya, TURKEY

**Abstract:** Freestanding tin oxide-boron oxide/reduced graphene oxide ($SnO_2$-$B_2O_3$/rGO) nanocomposite anode was produced for Li-ion cells. This binder-free flexible paper anode structure was fabricated by combining $SnO_2$-$B_2O_3$ composite and graphene oxide which were synthesized through the sol–gel method and Hummers' method, respectively. Field emission gun scanning electron microscopy, high-resolution transmission electron microscopy, energy dispersive X-ray spectrometer, Fourier transform infrared spectroscopy, Raman spectroscopy, and X-ray diffraction were utilized to characterize anode materials. The Williamson-Hall (W-H) analysis was applied using XRD data to determine crystal size and strain of the lattice. Electrochemical tests, cyclic voltammetry, and electrochemical impedance spectroscopy measurements were performed to determine electrochemical properties of the anodes. The results indicated that the anode formed with $SnO_2$-$B_2O_3$ particles anchored on the rGO layers provided higher discharge capacity (838 mAh $g^{-1}$) than that of $SnO_2$/rGO (395 mAh $g^{-1}$) after 100 cycles. The electron-deficient nature of boron supplied an effective increase in electrochemical energy storage performance.

**Key words:** Binder-free paper anodes, $SnO_2$-$B_2O_3$/rGO nanocomposites, Li-ion battery, electrochemical characterization

## 1. Introduction

Lithium-ion batteries (LIBs) are used as main energy storage devices in various fields including communication, electronics, hybrid electric vehicles, and renewable energy [1]. Owing to their increased energy density and high electromotive force, the LIBs gained worldwide interest and are frequently used in mobile and portable electronic devices. Therefore, producing novel electrode materials in order to fulfill the requirements for batteries having improved cycle characteristics and higher energy densities has been of great interest recently [2,3].

Graphite is a commercially available anode material for LIBs with longer life cycle, relatively lower cost, and abundant supply. However, disadvantageous features such as having poor energy density (375 mAh $g^{-1}$) and security issues caused by lithium deposition [1] lead researchers to propose alternative anode materials [4].

Tin dioxide ($SnO_2$) is an n-type semiconductor having a broad optical band gap (3.6 eV). Its conductivity primarily arises from the oxygen vacancies due to its nonstoichiometric nature [5]. $SnO_2$ has a wide range of applications owing to its satisfactory chemical and electrical properties [6]. Furthermore, tin oxide-based

---

*Correspondence: hkose@sakarya.edu.tr

materials have high-energy density and constitute elevated theoretical discharge capacity (1491 mAh g$^{-1}$) for LIBs. Regarding its unique characteristics, $SnO_2$ is a vigorous candidate to be used in LIBs as an anode material, instead of commercial graphite [5,7].

$SnO_2$ anode material, however, undergoes huge volume expansion and agglomeration of tin nanoparticles during alloying and dealloying process of Sn with $Li^+$. Accordingly, the pulverization and electrical detachment of active material occur at the anode [8]. Thus, development of nanostructured electrode materials with smaller internal strains and shorter lithium diffusion lengths contributes stabilizing the anode structures and avoiding the abovementioned issues [9,10].

Nevertheless, efforts of synthesizing new tin oxide nanostructures are not sufficient to enhance the cycle-life of $SnO_2$-based electrodes [9]. Placing carbon or other conductive materials at the tin oxide anode is another way to reduce the change in volume [11]. Graphene, a novel two-dimensional sheet of sp$^2$-hybridized carbon, has been widely used to support metal or metal oxides in order to improve the electrochemical performances of anode materials since it possesses and extraordinary electrical conductivity, large specific surface area, extensive mechanical flexibility, and elevated chemical and thermal/stability [12,13]. In particular, using this graphene structure as a buffer constitutes assembling the cell and the preparation of the electrodes in terms of eliminating the current collector, binder material, and slurry solvent [14].

Alternatively, $B_2O_3$ has been used to support the reaction between $SnO_2$ and $Li^+$. Boron atoms may act as the electron-acceptor owing to their electron-deficient nature during the electron transfer process accompanied with lithium insertion. Thus, they enable insertion of more lithium ions into the $SnO_2$ structure [15]. As $B_2O_3$ provides mechanical support, boron atoms increase electron density and conductivity. In a previous study, $B_2O_3$-doped $SnO_2$ structure has been used to produce hollow [10] and core-shell [16], whereas the $SnO_2$-$B_2O_3$ nanocomposite corresponds to a high-capacity anode, due to the supporting effect of $B_2O_3$. In another study, $B_2O_3$-$SnO_2$-Graphene nanopowders were designed as anodes by including binder and conducting agent to a slurry anode [17].

In the present work, $SnO_2$-$B_2O_3$/rGO and $SnO_2$/rGO binder-free buckypaper nanocomposites were produced as freestanding anodes for LIBs. To investigate the effect of including $B_2O_3$ to $SnO_2$ structure in terms of the electrochemical capacity and stability, $SnO_2$/rGO anodes were produced with and without the presence of $B_2O_3$. Improving the internal resistance reduction, the proposed ternary composite as freestanding flexible paper anode without any binder is a novel accomplishment and has not been studied previously. To characterize structural and morphological features of the produced nanocomposites, we used field emission gun scanning electron microscopy (FEG-SEM), high resolution transmission electron microscopy (HRTEM), energy dispersive X-ray spectrometer (EDS), and X-ray diffraction (XRD) methods. Electrochemical characteristics of the freestanding anodes were determined by cyclic voltammetry (CV) and electrochemical impedance spectroscopy (EIS). Moreover, electrochemical performance tests of CR2016 coin cell type LIBs were conducted at 25 °C within a voltage range of 2.5–0.01 V.

## 2. Materials and methods

### 2.1. Preparation of $SnO_2$/rGO and $SnO_2$-$B_2O_3$/rGO nanocomposite anodes

The production of $SnO_2$/rGO and $SnO_2$-$B_2O_3$/rGO buckypaper nanocomposites is performed at three stages. Initially, Hummers' method was applied to produce graphite oxide from pretreated graphite powders [18]. For this process, oxidizing agents such as $NaNO_3$, $KMnO_4$, and $H_2O_2$ were treated with $H_2SO_4$ (98%) and

deionized water. The obtained graphite oxide was washed with distilled water, centrifuged until the pH value reached neutral, and dried at 60 °C in a vacuum oven.

The second step is the synthesis of $SnO_2$ and $SnO_2$-$B_2O_3$ nanopowders by the sol–gel method. To synthesize $SnO_2$-$B_2O_3$ nanopowders, 0.01 mol of $SnCl_2$.$2H_2O$ and $H_3BO_3$ were dissolved in 10 mL absolute ethanol and glycerin was added in this solution as gelating agent. Obtained gel structure was stirred for several hours, dried in an oven at 120 °C, and then grounded in a mortar. Calcination of the product was carried out at 500 °C in air for 2 h applying a heating rate of 2 °C/min. $SnO_2$ was then synthesized in the absence of $H_3BO_3$, as well.

The final stage was the production of reduced graphene oxide and its nanocomposites with $SnO_2$ and $SnO_2$-$B_2O_3$. Graphite oxide was synthesized by Hummer's method and ultrasonicated with the nanopowders to produce 1:1 weight ratio of $SnO_2$/GO and $SnO_2$-$B_2O_3$/GO. For this, 45 mg $SnO_2$ or $SnO_2$-$B_2O_3$ nanopowders were synthesized by sol-gel method and dispersed with 45 mg graphite oxide in 50 mL of deionized water and ultrasonicated for another 2 h. Then, the suspension was vacuum-filtrated on PVDF membrane (Millipore, Durapore Membrane) and the nanocomposite papers of $SnO_2$/GO and $SnO_2$-$B_2O_3$/GO were peeled from it. Finally, freestanding $SnO_2$/rGO and $SnO_2$-$B_2O_3$/rGO nanocomposites were obtained after reduction in distilled hydrazine solution as shown in Figure 1a and used as anode in CR2016 Li-ion cell.
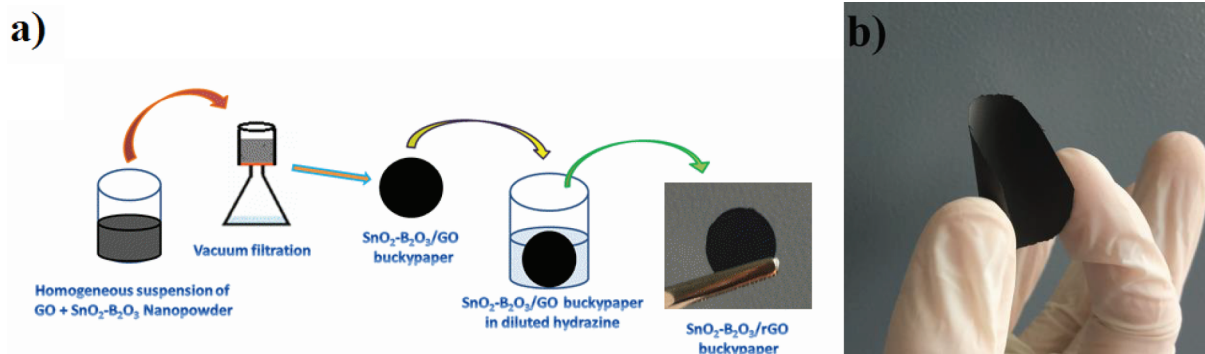


**Figure 1**. (a) Production of binderless freestanding $SnO_2$-$B_2O_3$/rGO buckypaper composite anode and (b) flexible $SnO_2$-$B_2O_3$/rGO composite anode.

## 2.2. Characterization of materials

To examine the morphology of the freestanding nanocomposites, FEG-SEM (FEI Quanta 450 FEG) and HRTEM (JEOL 2100) were performed. Composite elemental mapping was performed by EDS attached to the FEG-SEM. The crystal structures of the samples were analyzed by Rigaku D/MAX/2200/PC model device XRD with CuK$\alpha$ radiation ($\lambda$ = 1.54050 Å) having 1°/ min scanning speed. The W-H analysis was fulfilled using XRD data to calculate crystal strain and size. Optic measurements were conducted by FT-IR (Spectrum Two model PerkinElmer FT-IR) and Raman spectroscopy (RAMANRXN SYSTEMS).

## 2.3. Electrochemical analysis of the cells

To assemble CR2016 cells in a glove box (MBraun-Labstar), binder-free flexible $SnO_2$/rGO and $SnO_2$-$B_2O_3$/rGO buckypaper nanocomposite anodes were used as working electrode. Metallic lithium and polypropylene (PP) were used as cathode and separator, respectively. The commercial electrolyte consisting of a 1.0 M

solution of $LiPF_6$ was dissolved in a mixture of 1:1 volumetric ratio of ethylene carbonate and dimethyl carbonate and used as the electrolyte. Within the voltage range from 2.5 V to 0.01 V, the obtained cells were charged and discharged at room temperature under a constant current density on a BST8-MA MTI model battery tester with 0.2C cycling rate for 100 cycles. To determine the electrochemical behavior of the anodes, CV measurement was applied at the scan rate of 0.1 mVs$^{-1}$ within the same voltage range. EIS was also conducted by OrigaFlex OGF500 model OrigaLys ElectroChem SAS over a frequency range of 1000–0.01 Hz applying 10 mV amplitude.

## 3. Results

### 3.1. Structural characterization

To obtain $SnO_2$/rGO and $SnO_2$-$B_2O_3$/rGO nanocomposites, structural components were produced and then combined. Vacuum filtration production of binderless freestanding $SnO_2$-$B_2O_3$/rGO buckypaper composite anode is shown in Figure 1a, while Figure 1b displays flexible paper as the final product. The papers peeled from the PVDF membrane indicate a flexible and freestanding nature as manifested in Figure 1b.

To define the morphology of the produced nanocomposite papers designed with the combination of graphene sheets and $SnO_2$-$B_2O_3$ nanopowders, FEG-SEM was used. Figure 2a shows a crosssectional SEM image of the rGO. Graphene sheets possess relevant porosity for Li$^+$ diffusion and improve the efficiency of Li-Sn alloying and dealloying. Additionally, mesoporous nature that is often required for buffer stress of the anode in Li batteries was obtained in order to provide homogeneously anchored nanoparticles on the layers [19]. Figure 2b monitors FEG-SEM image of spherical nanoparticles of the $SnO_2$-$B_2O_3$ powder with homogeneous distribution and size. This nanostructure represents clear nanoparticles around 20 nm size without any agglomeration. When the surface morphologies of the produced $SnO_2$/rGO and $SnO_2$-$B_2O_3$/rGO nanocomposites were examined, the nanopowders were clearly observed under the graphene surface as displayed in Figures 2c and 2d. As a result, the desired crack-free structure was obtained to prevent mechanical disintegration of the anode with along with a homogeneous distribution of $SnO_2$ and $SnO_2$-$B_2O_3$ nanoparticles, which confirms that the decoration of nanoparticles between graphene layers was successfully achieved. To further investigate and verify the morphology of $SnO_2$-$B_2O_3$/rGO composite, TEM analysis was performed. HRTEM image of $SnO_2$-$B_2O_3$/rGO shows a homogeneous structure with $SnO_2$-$B_2O_3$ composite particles anchored on the graphene surface (Figure 2e). Lattice fringes of $SnO_2$ (002) plane on $SnO_2$-$B_2O_3$/rGO structure are observed in Figure 2f with d-spacing of 0.26 nm. Figure 2g clarifies EDS elemental mapping with a typical FEG-SEM image along with a C, Sn, O, and B maps for the $SnO_2$-$B_2O_3$/rGO composite. Particle nucleation of $SnO_2$-$B_2O_3$ on the graphene sheets was proved by the mappings. Highly homogeneous distribution of C, Sn, B, and O elements and good penetration of Sn, B, and O into the graphene sheets are shown in Figure 2g. In addition, Sn and B atomic compositions were determined using EDS analysis found to be 18.89% and 8.47%, respectively. These results were highly compatible with the production molar percentages of $SnO_2$-$B_2O_3$/rGO composite.

FT-IR transmission spectroscopy analysis was carried out with samples given in Figure 3a. FTIR spectrum of GO indicates a broad stretching peak of –OH around 3000–3500 cm$^{-1}$ and stretching vibration bands of –C=O and –C-O at about 1740 and 1000 cm$^{-1}$, respectively. Functional group peaks were caused by the oxidative reactants used in the Hummers' method. After reducing GO to rGO, vibration peaks that belong to the functional groups mostly disappeared, in which FTIR spectra confirmed a successful rGO production. Additionally, the spectra of rGO and other samples with graphene exhibited –C=C stretching bands at 1600 cm$^{-1}$. $SnO_2$ bearing samples indicated broader bands at 500 and 700 cm$^{-1}$, which were related to the
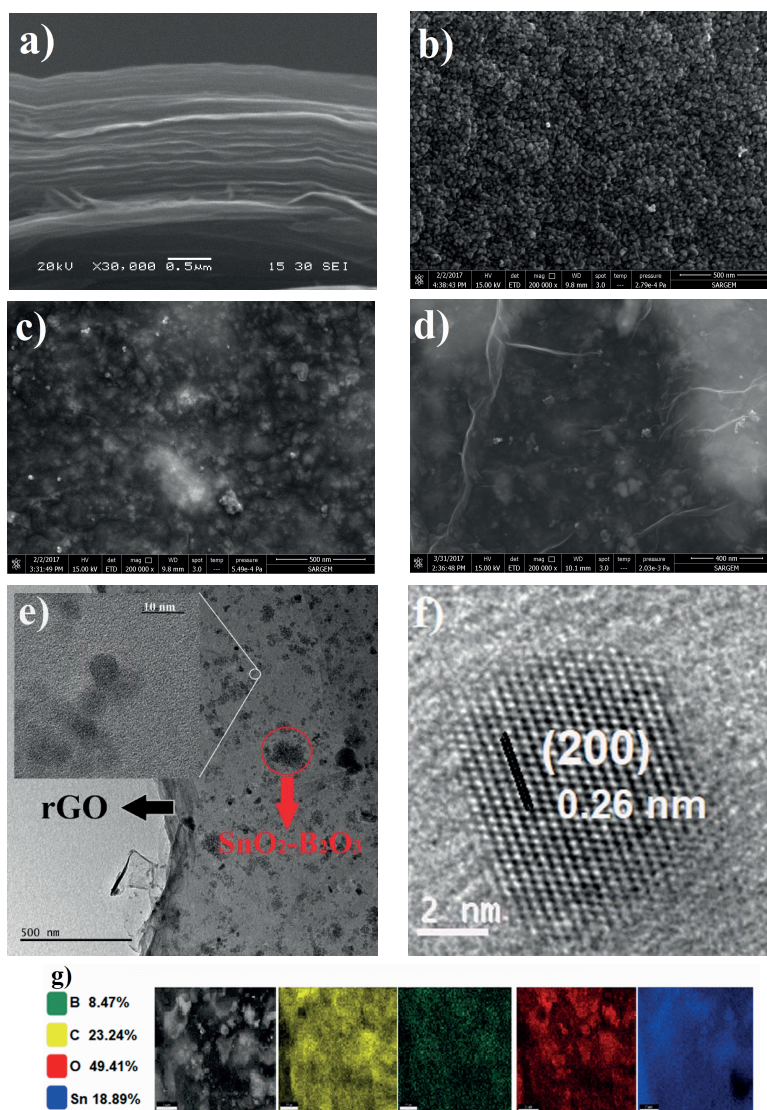
**Figure 2**. (a) Crosssectional SEM image of rGO. Surface FESEM images of (b) $SnO_2$-$B_2O_3$ nanopowders, (c) $SnO_2$/rGO, and (d) $SnO_2$-$B_2O_3$/rGO composite. HRTEM images of (e) $SnO_2$-$B_2O_3$/rGO, and (f) lattice fringes of (002) plane of $SnO_2$ in the structure of $SnO_2$-$B_2O_3$/rGO. (g) Elemental mapping of $SnO_2$-$B_2O_3$/rGO nanocomposite paper with the FEG-SEM image.

symmetric and asymmetric stretches of Sn–O–Sn bonds [5]. Comparing the spectra of pristine $SnO_2$, $SnO_2$-$B_2O_3$ powders, $SnO_2$-rGO, and $SnO_2$-$B_2O_3$-rGO composites, we observed that $B_2O_3$ containing samples displayed transmission bands around 700, 1200, and 1400 $cm^{-1}$, which could be assigned to the B–O bond vibrations in $BO_3$ units along with the Sn-O bands. These three spectral regions were comparable to borate glasses network. The first region yielded a bending peak at about 700 $cm^{-1}$, which was linked to B-O-B bonds. While the second one was pertaining to the B–O stretching in $BO_4$ units, that occurred between 800 and 1200 $cm^{-1}$, the asymmetric stretching peak of the B–O bonds in trigonal $BO_3$ units were at 1200–1600 $cm^{-1}$ and in the third region [20]. Consequently, FTIR analysis has verified the production of GO, rGO, and other samples with composite structure.
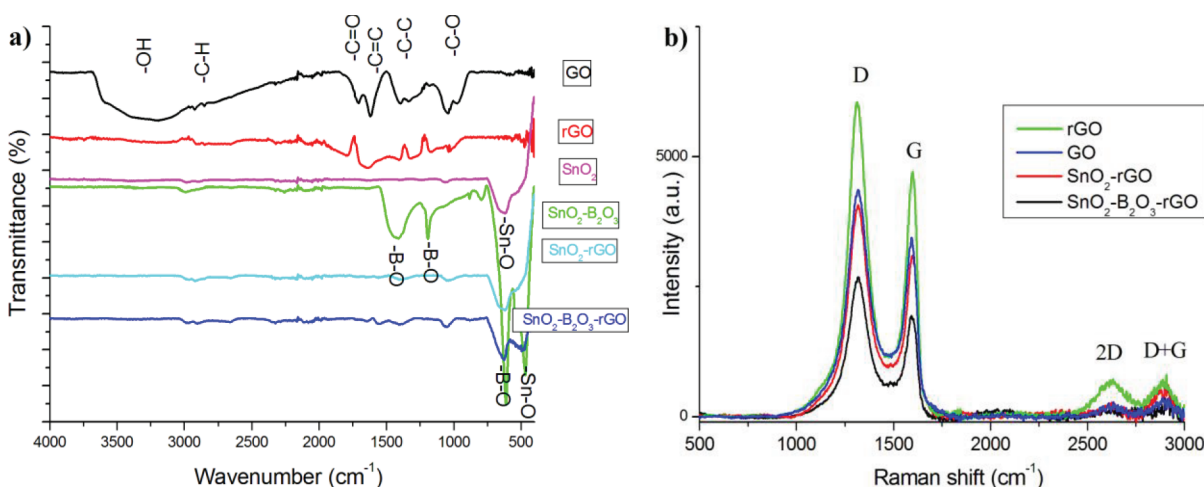
**Figure 3**. (a) FT-IR and (b) Raman spectra of the GO, rGO, and $SnO_2$-$B_2O_3$/rGO composite samples.

Figure 3b represents Raman spectra of GO, rGO, $SnO_2$/rGO, and $SnO_2$-$B_2O_3$/rGO. G and D bands of graphene were observed at 1590 and 1316 cm$^{-1}$, respectively, in which the G band was due to planar vibrations of the all sp$^2$ C atom pairs, whereas the D band was derived from regions with defects regions or disordered carbon sources. Likewise, the peaks at 2618 and 2899 cm$^{-1}$ were assigned to 2D and D + G bands. The 2D band might be attributed to the splitting of the electronic bands without necessitating any defects in the structure. Yet, similar to D-band, D + G band requires a defect for activation process with a close relation to D-band [21,22].

Disorder degree of graphene structure can be determined by intensity ratio of D to G band ($I_D/I_G$) using the Raman spectrum [22]. The $I_D/I_G$ values of GO, rGO, $SnO_2$/rGO, and $SnO_2$-$B_2O_3$/rGO were found to be 1.263, 1.286, 1.317, and 1.388, respectively, in which higher $I_D/I_G$ value corresponded to increased structural disorder of graphene and additional loading particles between graphene sheets. Here, $I_D/I_G$ value of rGO was found to be higher than that of GO since the reduction process caused structural disorder. Similarly, $SnO_2$/rGO and $SnO_2$-$B_2O_3$/rGO composites displayed naturally larger $I_D/I_G$ ratio than rGO owing to decorating particles between the layers. From the results, we conclude that $SnO_2$-$B_2O_3$/rGO nanocomposite bearing larger nanoparticles yields much disordered structure compared to $SnO_2$/rGO in terms of loading particles into graphene structure.

The crystal structure of the $SnO_2$-$B_2O_3$/rGO buckypaper nanocomposite was investigated through XRD analysis. Diffraction peaks of graphene oxide, reduced graphene oxide, pristine $B_2O_3$, pristine $SnO_2$ nanopowders, $SnO_2$-$B_2O_3$ nanopowders, and $SnO_2$-$B_2O_3$/rGO nanocomposite samples are given in Figure 4a. We detected the peak of graphene oxide around 11° [23]. Normally, graphite diffraction peak occurs around 26°; however, the peak shifted to 11° following oxidation. Reduced graphene oxide peaked at about $2\theta = 26°$ with (002) plane of carbon (JCPDS, 00-026-1080), which was obtained after reducing graphene oxide in hydrazine. Thus, the main peaks of graphene oxide and graphene were almost compatible with the previous knowledge [18,23]. High crystalline pristine $SnO_2$, $SnO_2$-$B_2O_3$, and $SnO_2$-$B_2O_3$/rGO composite structures indicated strong diffraction peaks corresponding to (110), (101), (200), and (211) planes near other weak peaks of cassiterite planes (JCPDS, 00-041-1445). Thus, for the $SnO_2$-$B_2O_3$/rGO sample, all of the diffraction peaks without carbon planes were about the planes of cassiterite type of $SnO_2$ crystal structure. For these composites, (002)

graphene and (001) $SnO_2$ plane diffraction peaks partially overlapped at about $2\theta = 26°$. As seen in the Figure 4a, pristine $B_2O_3$ yielded two broad diffraction peaks at $22.5°$ and $41.5°$, which might have stemmed from $B_2O_3$ single crystalline structure [17]. The $SnO_2$-$B_2O_3$ and $SnO_2$-$B_2O_3$/rGO structures also indicated these wide $B_2O_3$ diffraction peaks along with $B_2O_3$.
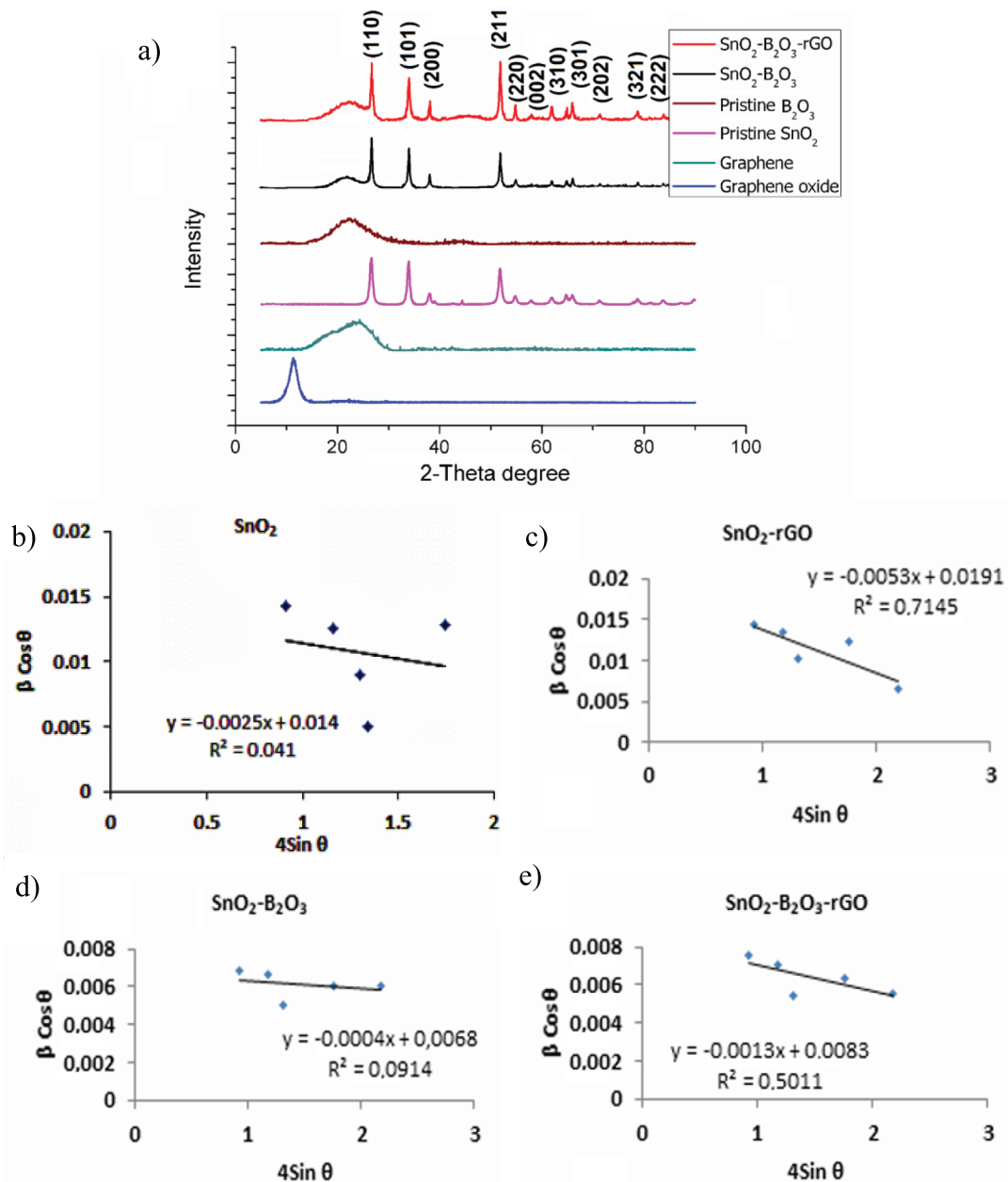


**Figure 4.** (a) XRD analyses of GO, rGO, pristine $SnO_2$, $B_2O_3$, $SnO_2$-$B_2O_3$ nanoparticles and $SnO_2$-$B_2O_3$/rGO nanocomposite buckypaper (bottom to top), W-H plots of (b) pristine $SnO_2$, (c) $SnO_2$/rGO, (d) $SnO_2$-$B_2O_3$, and (e) $SnO_2$-$B_2O_3$/rGO buckypaper nanocomposites.

To calculate crystallite size (D) and lattice strain ($\varepsilon$) of the $SnO_2$ in the pristine $SnO_2$, $SnO_2$-$B_2O_3$, $SnO_2$/rGO, and $SnO_2$-$B_2O_3$/rGO structures, the W-H method was applied to XRD outputs Equation (3), according to (110), (101), (200), (211), and (301) preferred orientation planes of $SnO_2$. This analysis

method is also named as uniform deformation model (UDM) which was derived from the coalescence of the Scherrer ($D = K\lambda/\beta_D\cos\theta$) and Stokes–Wilson equations ($\varepsilon_{str} = \beta_{str}/4\tan\theta$).

$$\beta_{hkl} = \beta_{str} + \beta_D \tag{1}$$

$$\beta_{hkl} = \left(\frac{K\lambda}{D\cos\theta}\right) + (4\varepsilon\tan\theta) \tag{2}$$

$$\beta_{hkl}\cos\theta = \left(\frac{K\lambda}{D}\right) + (4\varepsilon\sin\theta) \tag{3}$$

UDM formula was obtained by rearranging Eq. (2) as Eq. (3), where D is the mean crystallite size of crystalline structure, K is the shape factor (0.94), $\lambda$ is the X-ray wavelength (1.5406 Å), $\beta$ is the full width at half maximum (FWHM) of XRD peak, and $\theta$ is the Bragg angle.

Williamson-Hall plots were drawn according to Eq. (3) for the (110), (101), (200), (211), and (301) preferred orientation planes of $SnO_2$ in the pristine $SnO_2$, $SnO_2$/rGO, $SnO_2$-$B_2O_3$, and $SnO_2$-$B_2O_3$/rGO nanocomposite crystal structures, which could be examined in Figures 4b–4e, respectively. These plots possessed strain and particle size via the slope and y-intersect of the fitted lines, respectively. Here, the slope value of the equation represents crystallite strain ($\varepsilon$) and y-intersect corresponds to "$K\lambda/D$" value in the insets of Figure 4b–4e. As K (0.94) and $\lambda$ (0.154 nm) are constants, D can be easily calculated from obtained y-intersect values as nm. Strain originated from lattice deformation manifested negative values which may be due to the lattice shrinkage [24].

Table 1 represents the values of lattice strain and crystallite size of $SnO_2$ in nanocomposite structures, which were calculated using the W-H analysis. $SnO_2$/rGO indicated minimum crystallite size and maximum strain, while samples with $B_2O_3$ displayed larger nanoparticles and lower strains, concluding that crystallite size is inversely proportional with the strain [14]. Since smaller grain size provided stronger interaction with graphene layers, there had been an increase in the lattice strain. Interestingly, the effect of graphene on the samples were clearly noticed when the nanocomposite structures of $SnO_2$-$B_2O_3$ and $SnO_2$-$B_2O_3$/rGO were compared. Introduction of graphene in $SnO_2$-$B_2O_3$ structure increased strain due to shrinkage of the lattice, which in turn yielded smaller particles. This finding is associated with anchored composite particles on the surfaces of graphene sheets, confirming the FEG-SEM results. Obtained results from pristine $SnO_2$ and $SnO_2$/rGO nanocomposite provided similar outputs with $SnO_2$-$B_2O_3$ and $SnO_2$-$B_2O_3$/rGO.

**Table 1**. Crystallite size and lattice strain of the $SnO_2$ in the pristine $SnO_2$, $SnO_2$-rGO, $SnO_2$-$B_2O_3$, and $SnO_2$-$B_2O_3$/rGO composites, calculated from the W-H analysis.

| Sample name | $SnO_2$ | $SnO_2$-rGO | $SnO_2$-$B_2O_3$ | $SnO_2$-$B_2O_3$/rGO |
|---|---|---|---|---|
| D, nm | 10 | 7 | 20 | 16 |
| Strain | $-2.5 \times 10^{-3}$ | $-5.3 \times 10^{-3}$ | $-0.4 \times 10^{-3}$ | $-1.3 \times 10^{-3}$ |

As a result, the W-H analysis indicated compatible results with FEG-SEM morphological analysis. Likewise, interpreting the findings obtained from the W-H method and Raman spectra, we discovered that $SnO_2$-$B_2O_3$ crystal structure had lower lattice strains than $SnO_2$ in their rGO composites. On the other

hand, graphene structure had larger disorder for $SnO_2$-$B_2O_3$-rGO than $SnO_2$-rGO composite structure, which means that graphene structure highly accommodated the stress of $B_2O_3$ contained composite structure.

## 3.2. Electrochemical characterization

CV was carried out to investigate the electrochemical behavior of the $SnO_2$-$B_2O_3$/rGO nanocomposite anode comparing to $SnO_2$/rGO electrode during the charge/discharge process. Figures 5a and 5b represent CV curves of the $SnO_2$/rGO and $SnO_2$-$B_2O_3$/rGO nanocomposite anodes for 5 cycles. CV measurements for the alloying and dealloying mechanism of lithium with $SnO_2$ and graphene were conducted in the potential range of 2.5–0.01 V vs. $Li/Li^+$ at a scanning rate of 0.1 mV s$^{-1}$.
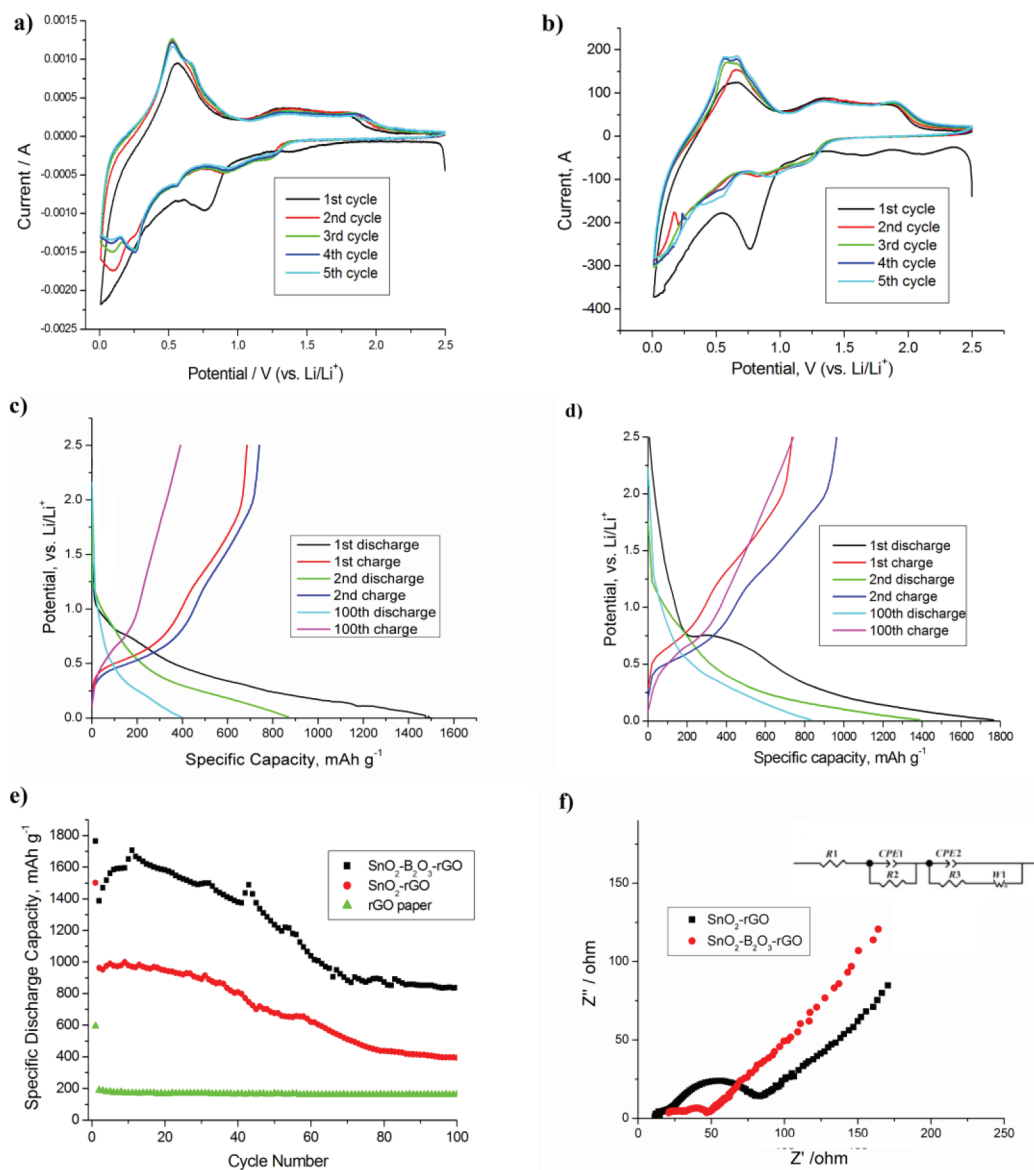


**Figure 5**. CV of (a) $SnO_2$/rGO, (b) $SnO_2$-$B_2O_3$/rGO anodes between 2.5–0.01 V for five cycles (0.1 mV s$^{-1}$ scan rate), the galvanostatic charge-discharge curves of (c) $SnO_2$/rGO and (d) $SnO_2$-$B_2O_3$/rGO buckypaper nanocomposite anodes at 0.2C for 1st, 2nd, and 100th cycles, (e) the comparison of cycling performance, (f) Nyquist plots of the cells after 100 charge/discharge cycles with the equivalent circuit model.

The following are the reactions of lithium with $SnO_2$ and carbon, which were observed in CV curves as reduction and oxidation peaks [25,26].

$$SnO_2 + 4Li^+ + 4e^- \ Sn + 2Li_2O \tag{4}$$

$$Sn + xLi^+ + xe^- Li_xSn(0 \leq x \leq 4, 4) \tag{5}$$

$$C_3 + xLi^+ + xe^- Li_xC_3 \tag{6}$$
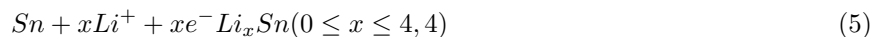
In Figures 5a and 5b, during the first discharge, the irreversible first reaction (4) was observed along with a reduction peak ($>1V$), forming amorphous $Li_2O$ and metallic Sn. Additionally, solely for the initial discharge, the sharp and wide peak could be observed at 0.75 V, resulting from the dissociation of the electrolyte and the formation of a solid electrolyte interface (SEI) film at the anode surface. For further cycles, the metallic tin and lithium yielded the reversible reaction (5), leading to the formation of Li-Sn alloys with the composition of $Li_{4.4}Sn$ [27]. Similarly, carbon and lithium formed $Li_xC_6$ with a reversible intercalation process following the first cycle. Thus, cathodic and anodic peaks exhibited two shoulder peaks for the reduction and oxidation reactions, as given by (5) and (6). Alloying and intercalating reactions were seen below 0.5 V in the cathodic curves, whereas the anodic peaks were observed around 0.5 V for the lithium deintercalation from graphene (6) and the lithium dealloying from $Li_xSn$ (5). Other peaks above 1.0 V indicated that the reaction given by Eq. (5) could be partially reversible [17]. CV curves in Figure 5b also demonstrated that $B_2O_3$ had not participated in the charge/discharge processes, as there were no other peaks other than that of Sn and $Li^+$ reactions.

Figures 5c and 5d exhibited the galvanostatic charge and discharge curves of $SnO_2$/rGO and $SnO_2$-$B_2O_3$/rGO buckypaper nanocomposite anodes for 1st, 2nd, and 100th cycles in the voltage range of 2.5–0.01 V vs. $Li^+$/Li at 0.2 C cycling rate, respectively. Following the initial discharge, since the first reaction was irreversible (4) and SEI layer was formed by the decomposition of the electrolyte [28], a capacity decline has occurred, as mentioned in the CV analysis. Figure 5c indicates larger irreversible capacity loss after the first discharge compared to Figure 5d. Here, it is concluded that the composite with $B_2O_3$ provided more effective SEI layer and smaller capacity fade, which may be attributed to the free electron density structure of $B_2O_3$. Similarly, during the first lithium insertion, the galvanostatic discharge curves showed a sharp drop and a plateau about 0.75 V in accordance with CV for both samples. Other plateaus in the discharge and charge curves for the first, second, and last cycles occurred at the same voltages with the CV, in correspondence with alloying and dealloying mechanisms.

The comparison of discharge capacities of the freestanding anodes is represented in Table 2 and Figure 5e. The specific discharge capacities were obtained for the first discharge of $SnO_2$-$B_2O_3$/rGO, $SnO_2$/rGO, and rGO anodes as 1766, 1501, and 595 mAh g$^{-1}$, respectively. Table 2 shows that the capacity loss after the first discharge was smaller for the $SnO_2$-$B_2O_3$/rGO compared to the other anodes, which was also observable in galvanostatic voltage curves (Figure 5d). $SnO_2$-$B_2O_3$/rGO indicated discharge capacity as high as 838 mAh g$^{-1}$, whereas $SnO_2$/rGO and rGO depicted 395 and 163 mAh g$^{-1}$ discharge capacities, respectively. Evaluating these results and Table 1, we noticed that reversible capacity retention of $SnO_2$-$B_2O_3$/rGO was much higher than that of $SnO_2$/rGO composite anode. After the second discharge, freestanding $SnO_2$-$B_2O_3$/rGO anode displayed a capacity increase up to the 12th cycle and eventually a decrease. This increment could be attributed to the low wetting of the electrodes and separator by electrolyte, as previously reported in Li-ion studies [29].

Both $SnO_2$-$B_2O_3$/rGO and $SnO_2$/rGO anodes revealed decreases between 40th cycle and 80th cycle, then after 80th cycle they demonstrated cycling stability.

**Table 2**. The discharge capacities of free-standing nanocomposite anodes for the 1st, 2nd, 50th, and 100th cycles.

| Sample name | 1st cycle $(mAhg^{-1})$ | 2nd cycle $(mAhg^{-1})$ | 50th cycle $(mAhg^{-1})$ | 100th cycle $(mAhg^{-1})$ |
|---|---|---|---|---|
| rGO | 595 | 188 | 169 | 163 |
| $SnO_2$/rGO | 1501 | 962 | 676 | 395 |
| $SnO_2$-$B_2O_3$/rGO | 1766 | 1388 | 1237 | 838 |

As a result, $SnO_2$-$B_2O_3$/rGO and $SnO_2$/rGO nanocomposite structures that were supported by graphene provided beneficial effects in terms of preventing mechanical disintegration and anode pulverization along with satisfactory discharge capacities as high as 838 and 395 mAh g$^{-1}$, respectively, after 100 cycles.

Although small particle size provides advantages such as the transport of electrons within the particles and large contact surface area with the electrolyte for high lithium ion transfer, very small particle size is undesirable due to the increased tendency to agglomeration between particles [30]. This also increases internal resistance. In light of this information, when the electrochemical results are examined, we might say that $SnO_2$-$B_2O_3$/rGO anode provides higher capacity as it exhibits proper size and stress. In addition, in this study, battery capacity cannot be evaluated solely with grain size and stress; it should be noted that the electrochemical contribution from the $B_2O_3$ structure is also noteworthy. Consequently, the $SnO_2$-$B_2O_3$/rGO composite anode indicated higher discharge capacity than $SnO_2$/rGO anode.

EIS was carried out to understand the electronical conductivity of the freestanding anodes. Nyquist curves of the samples were obtained using OrigaFlex OGF500 model OrigaLys Instrument. For the analysis, a sinewave of 10 mV amplitude was applied in a frequency range of 1000 kHz to 0.01 Hz. The Nyquist curve could be divided into 3 sections. High frequency region was the negative imaginary impedance part and is signified as electrolyte resistance ($R_s$ or $R_1$). In this region, $R_{sf}$ ($R_2$) also appeared as a semicircle and represented the contact resistance between SEI film and anode surface [31]. A semicircle at medium frequency indicated charge transfer resistance ($R_{ct}$ or $R_3$) and the kinetics of electrochemical battery reactions. The low-frequency part with 45° inclined lines was originated from boundaries in mass transfer. It is widely known as diffusion limited part and reflected Warburg resistance (W) as the diffusion of Li$^+$ ions in the solid. C was the capacitance of electrical double layer at the interface between the electrolyte and the electrode material [32,33].

Figure 5f represented the Nyquist plots of the nanocomposite freestanding anodes with an equivalent circuit model. Table 3 showed $R_s$, $R_{sf}$, and $R_{ct}$ resistance values of the anodes according to this model. $R_{ct}$ of 36 and 88 Ω were obtained for $SnO_2$-$B_2O_3$/rGO and $SnO_2$/rGO anodes, respectively. Comparing the EIS results of $SnO_2$-$B_2O_3$/rGO and $SnO_2$/rGO after 100 cycles, we discovered that $SnO_2$-$B_2O_3$/rGO had lower SEI film and charge transfer resistance. Collectively, $SnO_2$-$B_2O_3$/rGO provided easier charge/discharge transfer of Li$^+$ due to boron nature and increased electrochemical activity.

According to the results, $SnO_2$-$B_2O_3$/rGO and $SnO_2$-rGO nanocomposite anodes were obtained as freestanding flexible anodes sandwiching the particles between the graphene sheets. Here, highly conductive rGO was used as mechanical support to prevent volumetric expansion of $SnO_2$ particles, providing mesoporous nature. $B_2O_3$ also acted as a buffer; however, more importantly, it facilitated Li$^+$-Sn reaction by its electron-

**Table 3**. Impedance parameters of composite anodes, obtained after fitting with equivalent circuit.

| Sample | $R_s$ | $R_{sf}$ | $R_{ct}$ |
|---|---|---|---|
| $SnO_2$-$B_2O_3$-rGO | 80 | 19 | 36 |
| $SnO_2$-rGO | 49 | 49 | 88 |

acceptor structure. Thus, boron atoms enhanced the cycling capacity of the anode, increasing electron density and conductivity.

## 4. Discussion

Binder-free, elastic, and freestanding $SnO_2$/rGO and $SnO_2$-$B_2O_3$/rGO nanocomposite anodes were produced and compared in order to understand the effect of $B_2O_3$ addition in the anode structure. To do this, morphological, optical, and structural analyses were performed along with the electrochemical tests, which were conducted to determine the anode capacity. Analyses indicated that the structures of $SnO_2$/rGO and $SnO_2$-$B_2O_3$/rGO were obtained as architecture consisting of nanoparticles anchored on porous rGO nets, which was advantageous for high capacity Li-ion battery applications. Following 100 cycles, the electrochemical test results demonstrated high discharge capacities as 395 and 838 mAh g$^{-1}$ for $SnO_2$/rGO and $SnO_2$-$B_2O_3$/rGO anodes, respectively. Along with its elevated specific discharge capacity, $SnO_2$-$B_2O_3$/rGO also ensured high capacity retention and stability due to the effect of increased free-electron density of the anode structure by boron atoms. Consequently, through this method, $SnO_2$-$B_2O_3$/rGO porous structure was achieved by decorating nanoparticles between graphene layers. Additionally, high capacity, high stability, and long cycle-life anodes were obtained, proving the boron contribution to the anode structure, which in turn might be evaluated for advanced LIB applications.

## References

1. Yousaf M, Shi HTH, Wang Y, Chen Y, Ma Z et al. Novel pliable electrodes for flexible electrochemical energy storage devices: recent progress and challenges. Advanced Energy Materials 2016; 6: 1600490. doi: 10.1002/aenm.201600490

2. Derrien G, Hassoun J, Panero S, Scrosati B. Nanostructured Sn–C composite as an advanced anode material in high-performance lithium-ion batteries. Advanced Materials 2007; 19 (17): 2336-2340. doi: 10.1002/adma.200700748

3. Zhang WM, Hu JS, Guo YG, Zheng SF, Zhong LS et al. Tin-nanoparticles encapsulated in elastic hollow carbon spheres for high-performance anode material in lithium-ion batteries. Advanced Materials 2008; 20: 1160-1165. doi: 10.1002/adma.200701364

4. Larcher D, Beattie S, Morcrette M, Edstrom K, Jumas JC et al. Recent findings and prospects in the field of pure metals as negative electrodes for Li-ion batteries. Journal of Materials Chemistry 2007; 17: 3759-3772. doi: 10.1039/B705421C

5. Köse H, Karaal Ş, Aydın AO, Akbulut H. Structural properties of size-controlled $SnO_2$ nanopowders produced by sol–gel method. Materials Science in Semiconductor Processing 2015; 38: 404-412. doi: 10.1016/j.mssp.2015.03.028

6.  Ahn HJ, Choi HC, Park KW, Kim SB, Sung YE. Investigation of the structural and electrochemical properties of size-controlled $SnO_2$ nanoparticles. Journal of Physical Chemistry B 2004; 108 (28): 9815-9820. doi: 10.1021/jp035769n

7.  Park MS, Wang GX, Kang YM, Wexler D, Dou SX et al. Preparation and electrochemical properties of $SnO_2$ nanowires for application in lithium-ion batteries. Angewandte Chemie 2007; 119 (5); 764-767.
    doi: 10.1016/j.matchar.2012.11.011

8.  Fan J, Wang T, Yu CZ, Tu B, Jiang ZY et al. Ordered, nanostructured tin-based oxides/carbon composite as the negative-electrode material for Lithium-ion batteries. Advanced Materials 2004; 16 (16): 1432-1436. doi: 10.1002/adma.200400106

9.  Zhang C, Peng X, Guo Z, Cai C, Chen Z et al. Carbon-coated $SnO_2$/graphene nanosheets as highly reversible anode materials for lithium ion batteries. Carbon 2012; 50: 1897-1903. doi: 10.1016/j.carbon.2011.12.040

10. Liu R, Li D, Tian D, Xia G, Wang C et al. Promotional role of $B_2O_3$ in enhancing hollow $SnO_2$ anode performance for Li-ion batteries. Journal of Power Sources 2014; 251: 279-286. doi: 10.1016/j.jpowsour.2013.11.068

11. Lou XW, Chen JS, Chen P, Archer LA. One-Pot Synthesis of Carbon-Coated $SnO_2$ Nanocolloids with Improved Reversible Lithium Storage Properties. Chemistry Materials 2009; 21 (13): 2868-2874. doi: 10.1021/cm900613d

12. Lian P, Zhu X, Liang S, Li Z, Yang W et al. Large reversible capacity of high quality graphene sheets as an anode material for lithium-ion batteries. Electrochimica Acta 2010; 55: 3909-3914. doi: 10.1016/j.electacta.2010.02.025

13. Qin J, He C, Zhao N, Wang Z, Shi C et al. Graphene Networks Anchored with Sn@Graphene as Lithium Ion Battery Anode. ACS Nano 2014; 8 (2): 1728-1738. doi: 10.1021/nn406105n

14. Köse H, Karaal Ş, Aydın AO, Akbulut H. A facile synthesis of zinc oxide/multiwalled carbon nanotube nanocomposite lithium ion battery anodes by sol-gel method. Journal of Power Sources 2015; 295: 235-245.
    doi: 10.1016/j.jpowsour.2015.06.135

15. Xiang HQ, Fang SB, Jiang YY. Carbons prepared from boron-containing polymers as host materials for lithium insertion. Solid State Ionics 2002; 148: 35-43. doi: 10.1016/S0167-2738(02)00108-X

16. Xia G, Li N, Li D, Liu R, Xiao N et al. Preparation of novel $SnO_2$–$B_2O_3$ core–shell nanocomposite and their lithium storage ability. Materials Letters 2012; 79: 58-60. doi: 10.1016/j.matlet.2012.03.079

17. Wen L, Qin X, Meng W, Cao N, Song Z. Boron oxide–tin oxide/graphene composite as anode materials for lithium ion batteries. Materials Science and Engineering: B 2016; 213: 63-68. doi: 10.1016/j.mseb.2016.05.004

18. Cetinkaya T, Ozcan S, Uysal M, Guler MO, Akbulut H. Free-standing flexible graphene oxide paper electrode for rechargeable Li-$O_2$ batteries. Journal of Power Sources 2014; 267: 140-147. doi: 10.1016/j.jpowsour.2014.05.081

19. Mukherjee R, Krishnan R, Lu TM, Koratkar N. Nanostructured electrodes for high-power lithium ion batteries. Nano Energy 2012; 1: 518-533. doi: 10.1016/j.nanoen.2012.04.001

20. Ardelean I, Cora S. FT-IR, Raman and UV–VIS spectroscopic studies of copper doped $3Bi_2O_3.B_2O_3$ glass matrix. Journal of Materials Science: Materials in Electronics 2008; 19: 584-588. doi: 10.1007/s10854-007-9393-3

21. Ni ZH, Yu T, Lu YH, Wang YY, Feng YP et al. Uniaxial strain on graphene: raman spectroscopy study and band-gap opening. ACS Nano 2008; 2 (11): 2301-2305. doi: 10.1021/nn800459e

22. Ferrari AC. Raman spectroscopy of graphene and graphite: Disorder, electron–phonon coupling, doping and nonadiabatic effects. Solid State Communications 2007; 143: 47-57. doi: 10.1016/j.ssc.2007.03.052

23. Kucinskis G, Bajars G, Kleperis J. Graphene in lithium ion battery cathode materials: A review. Journal of Power Sources 2013; 240: 66-79. doi: 10.1002/er.4223

24. Zak AK, Abd Majid WH, Abrishami ME, Yousefi R. X-ray analysis of ZnO nanoparticles by Williamson-Hall and size-strain plot methods. Solid State Sciences 2011; 13: 251-256. doi: 10.1016/j.solidstatesciences.2010.11.024

25. Lu X, Wu G, Xiong Q, Qin H, Ji Z et al. Laser in-situ synthesis of $SnO_2$/N-doped graphene nanocomposite with enhanced lithium storage properties based on both alloying and insertion reactions. Applied Surface Science 2017; 422: 645-653. doi: 10.1016/j.apsusc.2017.06.052

26. Tian L, Zhuang Q, Li J, Shi Y, Chen J et al. Mechanism of intercalation and deintercalation of lithium ions in graphene nanosheets. Chinese Science Bulletin 2011; 56 (30): 3204-3212. doi: 10.1007/s11434-011-4609-6

27. Köse H, Dombaycıoğlu Ş, Aydın AO, Akbulut H. Production and characterization of free-standing $ZnO/SnO_2$/ MWCNT ternary nanocomposite Li-ion battery anode. International Journal of Hydrogen Energy 2016; 41: 9924-9932. doi: 10.1016/j.ijhydene.2016.03.202

28. Köse H, Aydin AO, Akbulut H. Sol–gel preparation and electrochemical characterization of $SnO_2$/MWCNTs anode materials for Li-ion batteries. Applied Surface Science 2013; 275: 160-167. doi: 10.1016/j.apsusc.2013.01.055

29. Dombaycıoğlu Ş, Köse H, Aydın AO, Akbulut H. The effect of $LiBF_4$ salt concentration in EC-DMC based electrolyte on the stability of nanostructured $LiMn_2O_4$ cathode. International Journal of Hydrogen Energy 2016; 41: 9893-9900. doi: 10.1016/j.ijhydene.2016.03.165

30. Bruce PG, Scrosati B, Tarascon JM. Nanomaterials for Rechargeable Lithium Batteries. Angewandte Chemie International Edition 2008; 47: 2930-2946. doi: 10.1002/anie.200702505

31. Fan X, Jiang A, Dou P, Ma D, Xu X. Three-dimensional ultrathin Sn/polypyrrole nanosheets network as high performance lithium-ion battery anode. RSC Advances 2014; 4: 52074-52082. doi: 52082. 10.1039/C4RA09114K

32. Pacios M, Marti n-Ferna ndez I, Villa R, Godignon P, Del Valle M, Bartrolí J, Esplandiu MJ. Carbon nanotubes as suitable electrochemical platforms for metalloprotein sensors and genosensors. In: Naraghi M. (editor). Carbon Nanotubes–Growth and Applications, Rijeka, Croatia: InTech, 2011, pp. 299-324.

33. Jespersen JL, Tønnesen AE, Nørregaard K, Overgaard L, Elefsen F. Capacity measurements of Li-ion batteries using AC impedance spectroscopy. World Electric Vehicle Journal 2009; 3: 127-133. doi: 10.3390/wevj3010127